# Visible to Near-Infrared Sensitization of Silicon Substrates *via* Energy Transfer from Proximal Nanocrystals: Further Insights for Hybrid Photovoltaics

Michael T. Nimmo,[†] Louis M. Caillard,[‡] William De Benedetti,[‡] Hue M. Nguyen,[†] Oliver Seitz,[‡] Yuri N. Gartstein,[†] Yves J. Chabal,[‡] and Anton V. Malko[†,*]

[†]Department of Physics and [‡]Department of Materials Science, The University of Texas at Dallas, Richardson, Texas 75080, United States

ABSTRACT We provide a unified spectroscopic evidence of efficient energy transfer (ET) from optically excited colloidal nanocrystal quantum dots (NQDs) into Si substrates in a broad range of wavelengths: from visible (545 nm) to near-infrared (800 nm). Chemical grafting of nanocrystals on hydrogenated Si surfaces is achieved *via* amine-modified carboxy-alkyl chain linkers, thus ensuring complete surface passivation and accurate NQD positioning. Time-resolved photoluminescence (PL) has been measured for a set of CdSe/ZnS and CdSeTe/ZnS NQDs of various sizes and compositions grafted on Si and SiO_2 substrates. The measured acceleration of the PL decays on Si substrates is in good agreement with theoretical expectations based on the frequency-dependent dielectric properties of Si and NQD—Si separation distances. A comparative analysis reveals separate contributions to ET coming from the nonradiative (NRET) and radiative (RET) channels: NRET is a dominant mechanism for proximal NQDs in the middle of the visible range and becomes comparable with RET toward near-infrared wavelengths. The broad range over which the ET efficiency is estimated to be at the level of ~90% further supports the concept that hybrid nanocrystal/silicon thin-film photovoltaic devices could efficiently harvest solar energy across the entire spectrum of wavelengths.
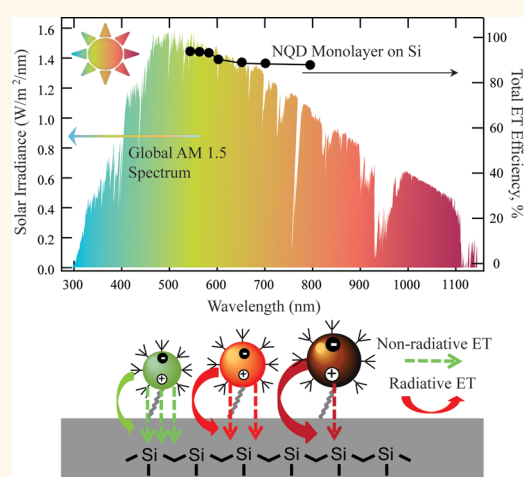
KEYWORDS: hybrid nanostructures · solar cells · energy transfer · silicon substrates · semiconductor nanocrystals

Harvesting solar energy is an important objective to fulfill the ever-growing energy demand. As a result, several new types of solar cells (SCs) have been introduced and discussed over the last two decades based on materials and principles that are quite different from the original crystalline Si p-n junction cell.[1−4] The quest for higher efficiency and lower production cost SCs with extended lifetime and versatile applications is driving the research. Despite much progress, many of these new approaches are yet to reach conceptual and operational maturity. The actual photovoltaic (PV) module production nowadays continues to overwhelmingly rely on Si technology. While some single- and multi-junction devices exhibit record efficiencies, the efficiencies of most of the manufactured SCs remain in the 10−18%

range, well below the thermodynamic limits for the photovoltaic conversion.[4] Hence, there is a well-recognized need and continuing effort to explore more opportunities to improve different aspects and/or achieve certain goals of SC performance and operation. According to an interesting recent viewpoint,[4] such opportunities may lie not only within the realm of the so-called third-generation photovoltaics[1,2] (multiple-carrier generation, up- and down-conversion, *etc.*) but also within a more familiar framework of a single-band-gap SC when combined with modern advances in the control of light and material processing.

Nanostructured materials attract considerable attention as candidates for PV devices. Among them, inorganic colloidal nanocrystal quantum dots (NQDs) have gained large popularity as photon absorbers owing to their

large absorption cross sections, photostability, tunability of the absorption edge *via* size-dependent quantum confinement, and ease of chemical manipulation and production. We have recently demonstrated[5] that photoexcited NQDs can also serve as efficient energy donors for adjacent ultrathin Si nanomembranes. Hybrid nanostructures combining NQDs with crystalline Si layers thus offer a potential for development of thin-film PV devices that take advantage of beneficial properties of both components. The excitonic sensitization of Si layers *via* energy transfer (ET) from strongly absorbing NQDs eliminates the issue of the weak solar light absorption in indirect band gap Si as a defining factor for the device thickness. At the same time, one can exploit the maturity of Si technologies to reliably and inexpensively manufacture high-carrier-mobility Si components for charge separation and transport.

Achieving high efficiency in SCs demands the effective use of the full solar spectrum, that is, harvesting photons of all energies, including those in the near-infrared (NIR) that account for ∼37% of the Sun's photon flux. (The NIR content becomes ∼27% for the photons with energies above the band gap of Si.) NQDs with the absorption onset at 1.2−1.3 eV would match conditions for the maximum conversion efficiency in a single-band-gap SC.[1] First infrared colloidal NQD SCs were reported in 2005,[6] and since then, their power conversion efficiencies have increased to the current level of 8%.[7] These SCs rely on the traditional charge transfer scheme putting extra demands on the carrier transport in the NQD network. Consequently, they suffer from insufficient interface quality issues manifested in a large number of defect sites that trap charge carriers, leading to poor transport through inhomogeneous NQD media. While tremendous progress has been achieved trying to mitigate these obstacles (various ligand exchange protocols to suppress surface states and enhance the electron mobility, mesoscopic TiO_2/ZnO substrates for more efficient charge collection), the resulting efficiency has not yet achieved technologically required levels.

Given these issues, the utilization of infrared NQDs in ET-based PV hybrids presents an attractive alternative. Charge carrier transport *via* NQDs (relying on overlap of the electronic wave functions) would no longer be required while energy transfer processes (relying on purely electromagnetic interactions) could be effective. Sensitization of Si layers in the NIR would boost the overall conversion efficiency. It is therefore important to understand the relevant ET processes, particularly ET from NQDs into Si in this region of the spectrum, to assess the viability of the concept and its practical realization. Recent experiments with PbS NQDs[8,9] indicate the existence of ET into Si materials at wavelengths $\lambda \sim 900$ nm.

In our previous studies of ET from colloidal CdSe/ZnS NQDs (middle part of the visible spectrum at the
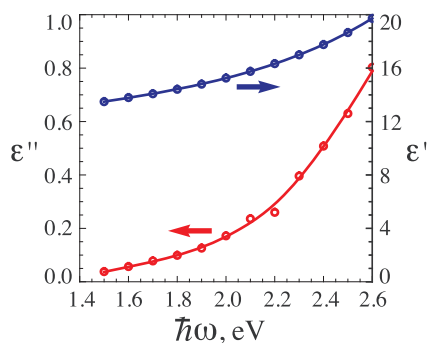
Figure 1. Frequency-dependent dielectric function $\varepsilon(\omega) = \varepsilon'(\omega) + i\varepsilon''(\omega)$ of crystalline Si as measured by Aspnes and Studna.[13] Dots show the reported tabulated data points, and solid lines display a smoothing-spline fit that is used in calculations for this paper.

wavelength $\lambda \sim 560$ nm) into bulk[10] and thin-layer[5] crystalline Si, we identified and distinguished two ET mechanisms. The nonradiative energy transfer (NRET) corresponds to the direct production of electron−hole pairs[11] in Si by the oscillating electrostatic-like dipole field of NQD excitons. In the radiative energy transfer (RET) process, the NQD excitons preferentially decay into photonic modes that propagate only within Si (those would become waveguiding modes in thin layers[12]). A different character of these processes is reflected in their specific dependence on the system parameters, particularly their distance from the substrate. NRET is estimated to be effective over distances of a few nanometers, while RET can be considerably longer-ranged and effective up to distances of ∼0.1λ (λ being the vacuum wavelength). In the case of proximal CdSe/ZnS NQDs, we established that NRET dominates, and the combined efficiency of ET into Si was estimated to be ∼90%. We note that while observed[5,10] distance dependence of transfer rates is consistent with ET mechanisms, it is not compatible with a typical exponential dependence of charge transfer. The latter mechanism is evidently non-operative at large nonconductive separations of NQDs from the substrate in our system.

Two considerations should be taken into account for discussion of ET processes in the NIR: first, the physical size of NQDs emitting in the near-IR is typically larger, and NRET rates from larger NQDs decrease due to longer effective separation distances (see refs 14 and 15 for recent discussions of different aspects of size-dependent Förster NRET with NQD energy donors). Second, the dielectric properties of Si exhibit the frequency dependence with strongly decreasing absorption at longer wavelengths (see Figure 1). Just as the dipole−dipole interaction-mediated Förster ET between small species depends on the overlap between the emission spectrum of the energy donor and the absorption spectrum of the acceptor,[12] the rate of NRET into Si is proportional to the imaginary part $\varepsilon''(\omega)$ of the dielectric function of Si at the NQD emission frequency ω. One therefore would expect a substantial

reduction of NRET rates in the NIR. The efficiency of RET, on the other hand, is related to the high refractive index of Si, that is, to the real part $\varepsilon'(\omega)$ of its dielectric function. As the latter changes only slightly, the role of RET is expected[5] to increase in the NIR.

In this article, we present a detailed comparative study of ET into Si substrates from a set of NQDs of variable sizes and compositions that emit in a wide spectral range between 545 and 800 nm. Submonolayers of NQDs have been carefully grafted on Si and SiO$_2$ substrates under the same processing conditions, thus allowing for a unified picture to be drawn from experimental results supplemented by a theoretical analysis. The determination of NRET and RET rates is based on time-resolved measurements of the NQD photoluminescence (PL) decay. We find that all of the results are largely consistent with a basic theoretical picture of the modification of the electric dipole transition decay rate in the vicinity of the dielectric interface as determined by the dielectric properties and the distance to the interface.[12,16] Confirming our expectations, the relative role of NRET and RET processes into Si changes for proximal NQDs as a function of the emission frequency: while NRET dominates at shorter wavelengths, it becomes comparable with RET toward the NIR. At larger distances from Si substrates, RET is a primary mechanism. Importantly, the efficacy of ET processes is consistently observed over a practically wide region of the solar spectrum with broad range overall ET efficiencies estimated at the level of ~90%. Along with our earlier demonstration[5] of the robustness of ET into ultrathin nanomembranes, the current observations strongly support the viability of the concept of ET-based hybrid nanocrystal/silicon thin-film PV devices for efficient harvesting of solar energy across the spectrum of wavelengths.

RESULTS AND DISCUSSION

In our experiments, we prepare uniform submonolayer coverages of nanocrystals specifically grafted on Si and SiO$_2$ surfaces. We used NQDs grafted on bare crystalline Si wafer samples and on samples with a $d =$ 10 nm thick interfacial, thermally grown spacer layer of SiO$_2$ on top of the crystalline Si substrate. Samples with NQDs grafted on a thick, 2 μm, layer of the oxide on top of the original Si substrates (referred to as "glass" in this paper) were used as a reference. Grafting of a self-assembled monolayer (SAM) passivates the Si surface through Si−C bonding and provides functional head groups for the NQD attachment.[17−19] In addition, linker-assisted grafting allows for accurate NQD positioning at well-defined distances from the Si substrate, well-suited for our ET studies. A submonolayer of nanocrystals is then attached to the surface with a density of ~10^{11} cm^{-2} to minimize the interdot interaction effects. By introducing the SiO$_2$ spacer, we are
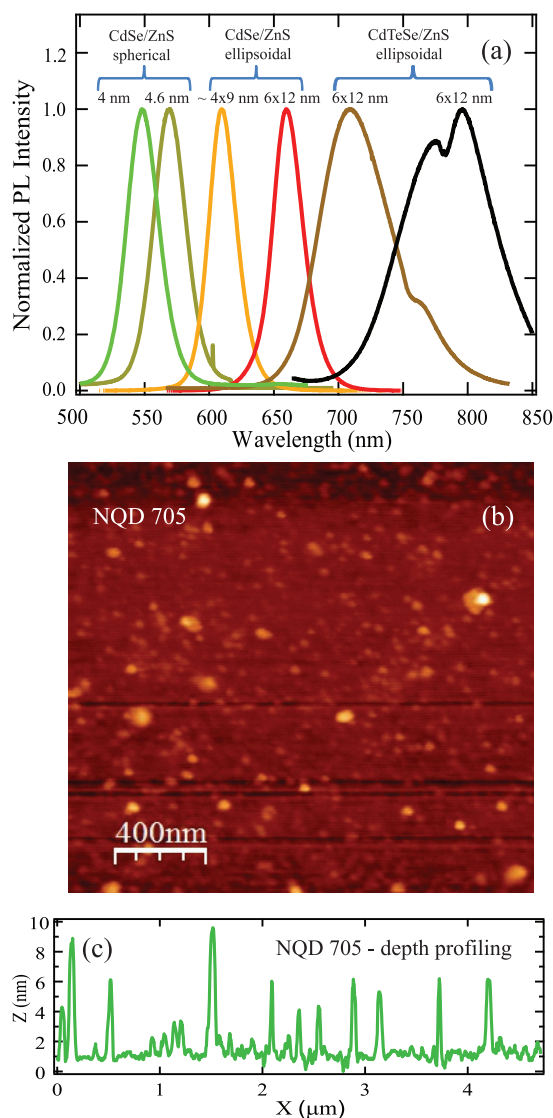
Figure 2. (a) PL emission spectra of different NQDs emitting from 545 to 800 nm as grafted on SiO$_2$. NQDs on Si exhibit the same PL profile. (b) AFM image of a sample with NQD-705 grafted on the Si surface. (c) AFM depth profiling extracted from (b) that indicates the preferential positioning of ellipsoidal NQDs with their longer axis parallel to the surface.

able to obtain a larger range of distances and therefore to affect the relationship between NRET and RET decay channels and thus to experimentally quantify both effects, as discussed later.

Figure 2a shows the PL emission spectra of a set of NQDs used in our experiments when grafted on glass substrates, covering a wide spectral region from 545 to 800 nm (2.3−1.55 eV). We label NQDs here by their peak emission wavelength λ: "NQD-λ". Of six NQD samples employed, two with the smallest sizes are spherical: CdSe/ZnS core/shell dots with diameters of $D =$ 4 nm (NQD-545) and $D =$ 4.6 nm (NQD-565). The other two are CdSe/ZnS dots of ellipsoidal shapes, with main axes of ~(4−5) × 9 nm (NQD-605) and 6 × 12 nm (NQD-655). The longer wavelength NQDs

(NQD-705 and NQD-800) are made of CdSeTe/ZnS with different Te concentrations, and both have an ellipsoidal shape, 6×12 nm. To better determine the NQD placement on the surface, we measured NQD positioning by atomic force microscopy (AFM) for ellipsoidal dots. A representative AFM image of larger dots (NQD-705) is shown in Figure 2b. Here we used a sample with a more dilute NQD surface coverage in order to accurately perform the AFM depth profiling displayed in Figure 2c. The profile shows that the majority of the ellipsoidal dots are positioned with their longer axis parallel to the surface, probably due to a larger number of linker molecules available for grafting in this geometry. The AFM measurements confirm that the smallest diameters of the ellipsoidal dots are very close to the values specified by the manufacturer, in this case $\sim 5.5-6$ nm (two larger spikes in the depth profile figure are likely from dots facing upward or from small clusters). The chemistry of our linkers ensures their direct attachment to the NQD body surface. Given the length of the grafting molecules, ~ 1.7 nm, we thus *estimate* NQD's center-to-surface separations as $z = 3.7$ nm for NQD-545, $z = 4$ nm for NQD-565, and $z \sim 4-5$ nm for NQD-605. The other three samples have approximately the same distance $z \sim 5-6$ nm (NQD-655, NQD-705, and NQD-800).

It is instructive to first assess the effects of the proximity to substrates on the NQD exciton decay within a well-known macroscopic electrodynamics framework.[12,16,20] The NQD exciton is described here as an effective point electric dipole emitter at the NQD center position, distance z from the substrate that takes into account both the physical size of the NQD and the grafting linker. The framework then treats the electric dipole transition decay *via* studies of the modification of electromagnetic fields of a classical oscillating electric dipole in dielectric environments characterized by their frequency-dependent complex dielectric functions $\varepsilon(\omega) = \varepsilon'(\omega) + i\varepsilon''(\omega)$. For weak exciton field coupling, the results obtained in the quantum picture of the exciton decay due to fluctuations of the electromagnetic field are identical to those obtained with classical dipoles (section 8.4 of ref 12). We used this picture in our previous work[5] and will briefly discuss some of its elements here for completeness and reader's convenience.

When in vacuum, the lifetime τ_0 and decay rate $\Gamma_0 = 1/\tau_0$ of the exciton due to radiative transitions are determined from[12]

$$\Gamma_0 = \frac{k^3 |\mathbf{p}|^2}{3\pi\varepsilon_0\hbar} \tag{1}$$

where $k = \omega/c = 2\pi/\lambda$ is the emission wavenumber and $\mathbf{p}$ the (effective) dipole transition moment. For the dipole positioned at distance z from a planar surface of the substrate, the electromagnetic decay rate is

modified to Γ, such that

$$\Gamma/\Gamma_0 = 1 + I(0, \infty) \tag{2}$$

$$I(a, b) = \text{Re} \int_a^b \frac{s\,ds}{2\sqrt{1 - s^2}} [(2s^2 - 1)r^{(p)}(s) + r^{(s)}(s)]\exp(2ikz\sqrt{1 - s^2}) \tag{3}$$

Here $r^{(s)}$ and $r^{(p)}$ are the reflection coefficients for s- and p-polarized waves, respectively, that contain the information on the dielectric function $\varepsilon(\omega)$ of the substrate. The decay rate of a dipole generally depends on its orientation; eq 3 is a result of averaging eq 10.26 of ref 12 over random dipole orientations. Upon reflection/refraction at the planar interface, the in-plane (parallel to the interface) components of the wave vector are conserved. The integration variable s in eq 3 relates magnitude $k_\parallel$ of those in-plane components to the vacuum wavenumber k as $k_\parallel(s) = sk$. Consequently, the normal components k_z of the wave vector in each of the spatial regions are determined by their dielectric functions:

$$k_{z1}^2(s) = (1 - s^2)k^2, \quad k_{z2}^2(s) = (\varepsilon - s^2)k^2 \tag{4}$$

in vacuum and in the substrate, respectively. Splitting the integration range in eq 2 into appropriate parts allows one, when possible, to distinguish between the "propagating" (real values of normal components in eq 4) and evanescent (imaginary values) character of the waves in different spatial regions.

For our numerical illustrations in Figure 3 and Figure 5, we directly compute integrals in eq 3 with the dielectric function $\varepsilon(\omega)$ of Si as shown in Figure 1. Note that while the reported experimental data on $\varepsilon'(\omega)$ in Si are consistent, the literature data on $\varepsilon''(\omega)$ in this spectral range feature variations, including by different measurement methods (see, *e.g.*, ref 21 for a comparison of some data). Panels a and b of Figure 3 show the ratio Γ/Γ_0 in eq 2 calculated for distances $z = 4$ and $z = 6$ nm from the dipole to the Si substrate as a function of the emission wavelength. These panels show the ratio not only for the total decay rate $\Gamma = \Gamma_{\text{Si}}$ but also for the contributions to it coming from different channels:

$$\Gamma_{\text{Si}} = \Gamma_\text{v} + \Gamma_{\text{RET}} + \Gamma_{\text{NRET}} \tag{5}$$

For the purposes of this paper, we define and denote these contributions by the following splitting of the integration range in eq 2:
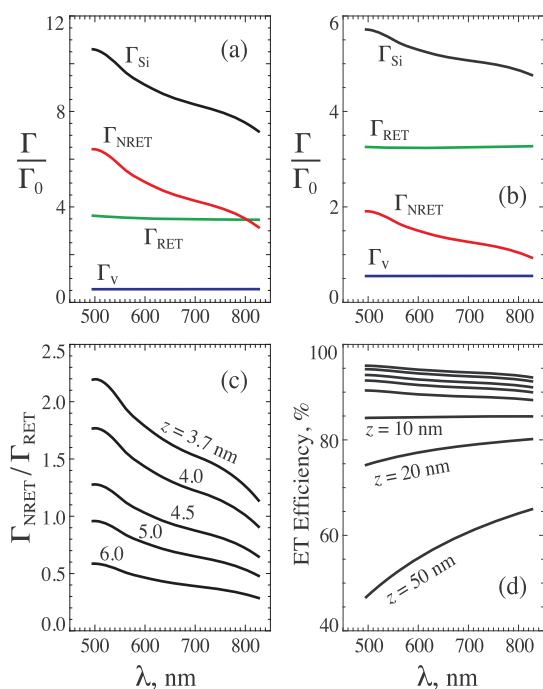
$$\Gamma_\text{v}/\Gamma_0 = 1 + I(0, 1) \tag{6}$$

$$\Gamma_{\text{RET}}/\Gamma_0 = I(1, \sqrt{\varepsilon'}) \tag{7}$$

$$\Gamma_{\text{NRET}}/\Gamma_0 = I(\sqrt{\varepsilon'}, \infty) \tag{8}$$

Given the weak absorption in Si in this spectral range, $\varepsilon'' \ll \varepsilon'$, the separation into channels eq 6–eq 8 is "clean", with the understanding that "propagating"

Figure 3. Theoretical results illustrating modification of the decay time as a function of vacuum wavelength for a randomly oriented electric dipole transition in the vicinity of the Si substrate described by the dielectric function $\varepsilon(\omega)$ of Figure 1. Top panels display the total decay rate and its contributions from different channels in terms of the vacuum rate: (a) for distance $z = 4$ nm and (b) $z = 6$ nm from the substrate. (c) Ratio of contributions from NRET and RET for a series of indicated distances from the substrate. (d) Corresponding total efficiencies of ET, eq 10, into the substrate for distances shown in panel c and, in addition, for larger separations as indicated.

modes also experience this weak absorption in Si. It is then clear from eq 4 that eq 6 corresponds to the decay into electromagnetic modes that can propagate in the whole space (both in vacuum and in Si). The contribution eq 7, on the other hand, corresponds to the electromagnetic modes that can propagate only inside Si, and the fields of these modes are evanescent on the vacuum side from the interface. These two contributions are *radiative*: they exist even when $\varepsilon'' = 0$ and practically do not change for small ε''. The contribution eq 8 is however very different: it would vanish for $\varepsilon'' = 0$ and is proportional to ε'' for the weak absorption, which is clearly seen in the analytical expression for its "electrostatic limit":[16,22]

$$\frac{\Gamma_{NRET}}{\Gamma_0} \simeq \left(\frac{\lambda}{2\pi z}\right)^3 \frac{\varepsilon''}{2|\varepsilon + 1|^2} \qquad (9)$$

There are no propagating electromagnetic modes corresponding to the range of variable s in eq 8; it describes a purely *nonradiative* process due to the Joule losses[22,23] in Si caused by the electrostatic-like near-field of the dipole.

It should be clear that contributions eq 7 and eq 8 describe decay channels corresponding to ET into Si:

eq 8 *via* direct excitation of the electron−hole pairs and eq 7 *via* the eventual absorption of the propagating modes in Si. In fact, a portion of Γ_v in eq 6 would also be absorbed in Si contributing to radiative ET. Keeping in mind the applications for ultrathin layers,[5] however, we do not add this contribution in the assessment of the efficiency and define RET here as exclusively due to exciton coupling with evanescent modes of the substrate, eq 7.

Panels a and b of Figure 3 show that Γ_v is suppressed in the vicinity of the substrate (a lower probability of decay into electromagnetic modes that can propagate in the whole space), while Γ_{RET} and Γ_{NRET} are substantial ensuring the overall acceleration of the decay with respect to vacuum. The relationship between NRET and RET changes as a function of distance z and wavelength λ, which is explicitly illustrated in panel c. It is clear that NRET dominates only in the visible part of the spectrum at shorter distances from Si. NRET becomes comparable to RET toward the NIR and is already overcome by RET at $z = 6$ nm over the whole spectral range shown here. Details of this relationship, of course, depend on numerical values of $\varepsilon(\omega)$ and are discussed here in the context of the data of Figure 1. A very different distance dependence of RET and NRET rates, however, does ensure the dominance of RET at sufficiently large distances from the substrate.

The analytical expression for NRET rate, eq 9, features a well-known $1/z^3$ distance dependence and is noteworthy for understanding why the decrease of Γ_{NRET}/Γ_0 toward longer wavelengths in numerical results of Figure 3 is milder than would be expected just from the behavior of ε'' in Figure 1. First, the dielectric screening factor $|\varepsilon + 1|^2$ in eq 9 becomes smaller toward the NIR. Second, it is not distance z itself, but the dimensionless z/λ ratio that is relevant for eq 9 (in other words, the vacuum radiative rate Γ_0 in eq 2 also becomes smaller for lower frequencies).

Consistent with our considerations above, we define the efficiency of ET into Si as the fraction

$$\frac{\Gamma_{RET} + \Gamma_{NRET}}{\Gamma_{Si}} \qquad (10)$$

which is shown in Figure 3d. Somewhat higher values would be obtained if a portion of Γ_v was added to RET that corresponds to the absorption in the substrate. In addition to displaying remarkably high resulting ET efficiencies for proximal dipoles, panel d also illustrates the efficacy of RET at much longer distances, such as the example of $z = 50$ nm. At distances z in excess of several nanometers, say $z \geq 10$ nm, NRET is a negligible process, while RET still contributes in a very substantial way. Characteristically, at larger distances z, RET is even more efficient in the NIR, the reason being smaller dimensionless ratios z/λ in that spectral region.

The described theoretical framework featured only electromagnetic decay channels; it can be easily modified
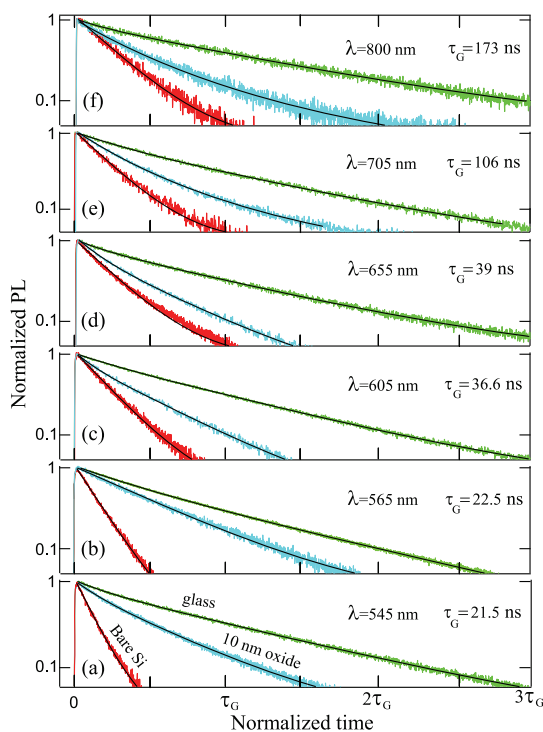
Figure 4. (a−f) PL dynamics for nanocrystals emitting at different wavelengths spanning the range from (a) 545 nm to (f) 800 nm. Shown on the panels are the respective PL measurement wavelengths. The horizontal scale (time) for each panel is normalized to the specific NQD lifetime (from double exponential fits) as measured on glass, τ_G, indicated on the panels, and extends to $t_{max} = 3\tau_G$. Green traces (top) show measured NQD PL decays on reference glass substrates, red traces (bottom) on bulk Si substrates, and light blue traces (middle) on Si substrates with a d = 10 nm thick interfacial SiO_2 spacer. Black curves on the top of the traces show the fits used to extract the lifetime values. A relative slowdown of the PL decays on Si substrates toward longer emission wavelengths is clearly visible.

by addition of another unspecified nonradiative decay channel that would correspond to quantum yields (QYs) of NQD emission less than 100%.[16] In the absence of the direct experimental data on QY, its value can be treated as a theoretical fitting parameter in comparison of experimental and theoretical results. With the same magnitude of QY < 100% for the decay in vacuum and in the vicinity of the substrate, theoretical results for the relative acceleration of the overall decay near the substrate would understandably (extra decay channel) exhibit lower values.

We will now discuss our experimental observations in the context of the theoretical framework. Time-resolved PL measurements have been conducted for various samples with all NQD types described above. We note here that while there is a general correspondence between the PL decay and PL intensity data, the absolute PL intensity is affected not only by ET but also by the optical generation rates as well as by the specifics of the emission collection. The interference effects in multilayered structures can modify the electric field intensity at the surface, thereby modifying the
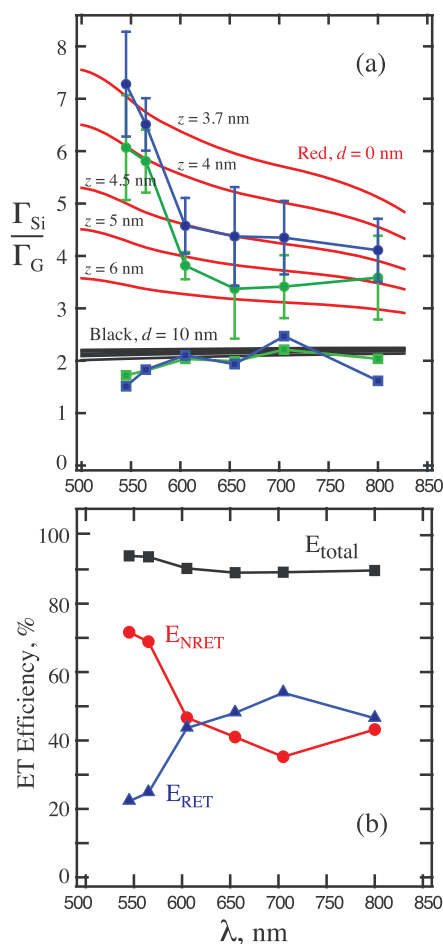
Figure 5. (a) Comparison of relative decay rates Γ_{Si}/Γ_G for different emission wavelengths as calculated from theory and as extracted from the PL decay data in Figure 4. For samples with NQDs on bare Si substrates: theoretical results shown as solid red lines for a set of dipole-to-substrate distances z; experimental data points with connected solid circles. For samples with NQDs on Si substrates with a d = 10 nm oxide spacer layer: theoretical results shown as solid black lines; experimental data points with connected solid squares. Blue- and green-colored data points represent different estimates for experimentally measured decay rates as extracted from, respectively, single/single and single/double fits to PL decays on bare Si and on glass substrates discussed in the text. Error bars represent mean square deviations for two or three independent sets of grafted NQD samples. (b) Total ET efficiency E_{total} shown by black squares along with separate contributions E_{NRET} from NRET (red circles) and E_{RET} from RET (blue triangles). The efficiencies were estimated as described in the text.

number of photogenerated NQD excitons. The radiative emission pattern is also well-known to depend on the geometry.[12] PL lifetime changes, on the other hand, depend only on the relevant decay rates such as ET. Thus, we uniformly employ changes in PL dynamics as a more unambiguous quantitative means for ET detection. Six panels a−f in Figure 4 show the time dependence of PL decays for six types of NQDs emitting at certain wavelengths (see Figure 2a). Each panel displays three traces: the PL decay for a reference sample with NQDs grafted on the glass substrate

(top trace, green), for a sample with NQDs grafted on the bare Si substrate (bottom trace, red), and for a sample where NQDs were grafted on the top of a $d = 10$ nm thick oxide layer separating NQDs from the bulk Si substrate (middle traces, light blue). In order to visually compare changes in the decay rates, the horizontal axis (time) for each panel is normalized to the measured decay time τ_G of the corresponding reference NQD-on-glass sample. The actual measured decay times on glass are indicated in the panels and range from $\tau_G = 21.5$ ns for small spherical ($D = 4$ nm) CdSe/ZnS dots to $\tau_G \sim 170$ ns for larger ellipsoidal (6×12 nm) CdSeTe/ZnS dots.

Lifetimes are generally well-fitted with monoexponential curves. However, some of the PL decays for NQDs grafted on SiO_2 surfaces exhibit small (10−15%) initial faster components. In a separate study, we have observed that such initial components can be considerably suppressed by passivating already grafted NQDs with diamine molecules on top. Such a behavior could be resultant from the less than perfect NQD grafting on SiO_2 surfaces as compared to the bare Si substrates, or it could originate from trapping channels specific to NQDs as have also been suggested in the literature for thiol-capped NQDs.[24] In instances with biexponential decay fits, the longer components of the decay have therefore been considered as lifetimes indicated in Figure 4.

It is transparent that the decays on bare Si substrates are much faster in comparison with decays on glass substrates—consistent with the picture of new decay channels due to ET from NQDs into Si. It is also clearly seen that decays on Si become progressively longer (with respect to the time-normalized reference traces) toward the NIR. This trend is also consistent with theoretical expectations of Figure 3 owing to a gradual reduction of NRET rates toward longer emission wavelengths. Measurements on samples with a thin $d = 10$ nm oxide spacer layer serve to assist in distinguishing effects due to NRET and RET decay channels. On the basis of theoretical calculations and on our previous work,[10] we expect that a 10 nm SiO_2 separation would make NRET into Si a negligible contribution while affecting radiative channels relatively insignificantly ($d/\lambda \sim 0.01−0.02$).

For a quantitative assessment and comparison with theoretical calculations, the PL lifetimes τ have been extracted from the data in Figure 4 and plotted in Figure 5a in terms of the corresponding decay rates ($\Gamma = 1/\tau$) relative to rates Γ_G on reference glass samples for each of the emission wavelength, respectively. Given some uncertainty in the fitting of the PL decays, the decay rates have been evaluated in two different ways: using single exponential fits to both PL decays on Si and on glass surfaces, and using single exponential fits on Si and longer components of the double exponential fits on glass surfaces as discussed above. Fits on Si are quite monoexponential across nearly two

decades of the PL signal change. Figure 5a shows the experimental data points evaluated in both ways for each type of NQDs as a function of their emission wavelength. Also plotted in Figure 5a are theoretical curves computed for dipole decay rates on bare Si and on Si with a $d = 10$ nm oxide spacer relative to decay on reference glass substrates (in computations, SiO_2 has been characterized by refractive index $n = 1.5$ across the whole spectral range).

Overall, there is a good agreement between salient features of experimental and theoretical results in Figure 5a. As a function of the wavelength, the results for NQDs on bare Si substrates exhibit a reduction from $\Gamma_{Si}/\Gamma_G \sim 6−7$ at $\lambda = 545$ nm to $\Gamma_{Si}/\Gamma_G \sim 4$ at $\lambda = 800$ nm. For NQDs on substrates with a $d = 10$ nm oxide spacer, on the other hand, there is little variation across the spectral range, with $\Gamma_{Si}/\Gamma_G \sim 2$. As the theoretical curves are shown for a set of different distances z from the dipole to the top surface, one can see that the data for NQDs on bare Si substrates is indeed reflective of larger NQD sizes toward the NIR and consistent with our estimates of z based on the sizes and linker lengths. Once again, there is very little dependence on z and NQD sizes in the data for substrates with the oxide spacer—as expected due to the suppressed NRET and relative insensitivity of Γ_{RET}/Γ_0 to the emission wavelength at these distances.

In fact, even quantitatively the agreement between experimental data and theoretical expectations in Figure 5a appears to be quite reasonable. With this in mind, one could now use experimental data in conjunction with theoretical results to estimate the efficiency of ET from NQDs into the Si substrate. Figure 5b shows the estimated total energy transfer efficiency E_{total} defined in eq 10 as well as separate contributions E_{RET} and E_{NRET} from RET and NRET processes, as a function of the wavelength for NQDs on bare Si substrates in our experiments. In these estimates of E_{total} from experimental data, we used theoretical values of $\Gamma_v \simeq 0.6\Gamma_0$ (see Figure 3) and $\Gamma_G \simeq 1.6\Gamma_0$ (see ref 5). Assuming now that Γ_{RET} does not change much for samples with a $d = 10$ nm oxide spacer layer, while NRET is practically negligible at these separations from the Si substrate, we directly use experimental data on samples with the spacer as a measure of Γ_{RET}. The resulting assessment of separate contributions E_{RET} and E_{NRET} to E_{total} is displayed in Figure 5b. It clearly shows that NRET dominates at shorter emission wavelengths in the visible but becomes comparable with RET toward longer wavelengths in the NIR. The joint contributions from both channels result in high efficiencies E_{total} across the whole spectral range, estimated at the level of $\sim$90%.

While precise numerical values for ET efficiency are of course subject to the accuracy of the data and adequacy of the model representation, it is important to realize that the fact of high ET efficiencies is clearly

borne out by the raw experimental data in Figure 5a. Even in the most "simple-minded" approach neglecting modifications of the reference radiative decay rates, that is assuming $\Gamma_G = \Gamma_0$ and $\Gamma_v = \Gamma_0$, the observation of $\Gamma_{Si}/\Gamma_G = 4$ would already mean $E_{total} = 75\%$, and the observation of $\Gamma_{Si}/\Gamma_G = 7$ would mean $E_{total} = 86\%$. Our estimates taking into account modifications of radiative decay rates in the vicinity of dielectric interfaces then understandably result in higher efficiency numbers.

We note that a generally good quantitative agreement between experimental and theoretical data has been achieved without usage of any extra fitting theoretical parameters, including that of QY. In fact, computational results with QYs appreciably smaller than 100% (the same QY for NQDs on Si and on SiO_2) show more substantial deviations from the experimental data. This is suggestive of high intrinsic QYs of NQDs in our submonolayers, which is consistent with other observations. The grafting technique passivates Si surface and hence eliminates trapping states that are usually the reason of decreased QY of NQDs on substrates. High QY is elucidated from long-time PL decays that are measured when NQDs are grafted on reference glass substrates—and these decays are very much comparable to PL lifetimes of NQDs in manufacturer solutions, with small differences that are directly attributable to somewhat different dielectric environments. The fact that a good agreement is achieved with high-QY theoretical calculations may indicate that emissive NQDs (that we study) do not possess any substantial intrinsic nonradiative channels. Experimental observations of lower QYs could then be rather interpreted as due to the conversion of emissive species into nonemissive (such as charged or trapped) excitons.

The very logic of the trends we observed in agreement with theoretical expectations indicates that the interplay of NRET and RET processes would be further tilted in favor of RET at longer wavelengths than studied here. In recent publications[8,9] on PbS NQDs ($\lambda \sim 900$ nm) deposited on various Si materials, however, the observed changes in PL dynamics have been attributed purely to the effects of NRET. We note that in experiments of ref 9, for example, NQDs were deposited on top of a $d = 5$ nm interfacial SiO_2 layer, thus resulting in at least a 7−8 nm separation from the NQD center to the Si substrate. Our results suggest that under such conditions NRET would be quite limited and ET may be mostly due to radiative coupling with electromagnetic modes propagating in Si. The interpretation of experimental data as entirely due to NRET effects would result in quite large values of the corresponding Förster radius—these surprisingly large values have already been noted[23] in the context of experiments in ref 8.

A proper evaluation of contributions from different channels to overall ET is relevant for design of ultrathin-film PV devices—it suffices to mention that while NRET is practically independent of the thickness of Si nanomembranes, the excitation of waveguiding modes via RET can be affected by that size.[5] Further improvements in that assessment should probably include both experimental and theoretical refinements. Experimentally, even better quality samples are desired exhibiting monoexponential PL decays. That would assist in model theoretical fits perhaps allowing one to distinguish between different radiating dipole orientations (the results in this paper have been averaged over random orientations). The theoretical framework also needs to be extended to evaluate the influence on our observations of dielectric local field effects for NQDs. It has been known for a long time that local field effects can substantially affect the magnitude of the effective dipole moment as seen in different uniform dielectric environments.[25] The corresponding influence of the uniform surrounding on the radiative lifetime of NQD excitons has become a subject of recent theoretical[26] and experimental[27] interest. How strongly similar effects would manifest themselves for NQDs in the interfacial region we study is not clear and requires a dedicated study.

As our observations here indicate an even larger role played by RET in the NIR spectral range, it is useful to compare this radiative coupling of NQD's PL emission with the coupling recently achieved in plasmonic-assisted nanostructures. There, surface-propagating plasmonic modes and in-coupling of the incident light into a semiconductor substrate have been realized with submicrometer-sized metal structures.[28] While such approaches certainly present interest for light manipulation and harvesting, we note that plasmonic modes can be inherently lossy, thus possibly reducing energy conversion efficiency. In our ET-based structures, the light conversion mechanism is implemented via photon absorption in the NQDs and coupling of the re-emitted light into propagating modes of the substrate. Given the broad absorption spectrum of semiconductor NQDs that can be tuned across visible and NIR spectral ranges, the majority of the incoming photons could be potentially converted into band edge excitons, which, in turn, are efficiently transferred into the Si substrate via combined effects of NRET and RET. The significance of RET becomes more accentuated at the NIR wavelengths where the absorption of crystalline Si is extremely weak. To our knowledge, the important role of RET in harvesting NIR photons in ET-based hybrid nanostructures have not been properly addressed so far, and this paper provides a first quantitative determination of the efficacy of this process for individual NQDs.

We already discussed[5] that device-oriented ET-based nanostructures need to employ optically thick, multilayer NQD assemblies to provide for sufficient

absorption of the incident light. These dense assemblies can substantially affect the local and global dielectric environment leading to changes in the interplay of NRET and RET processes, both between the NQDs and in their coupling with Si substrates. We foresee measurements of ET in macroscopically thick NQD layers grafted on Si substrates as the next important step in assessing the effectiveness of ET-based hybrid PV structures.

CONCLUSIONS

To summarize, we have demonstrated a hybrid system composed of colloidal nanocrystals and Si substrates that can effectively transfer optically created NQD excitations into high-carrier-mobility Si material over a wide wavelength range, from visible to the near-infrared. We employed covalent grafting of NQDs on crystalline Si substrates ensuring electronic passivation of surfaces and positioning NQDs at well-defined distances from the Si substrate. Observations and a quantitative analysis indicate very high broad range efficiencies of ET, estimated to be at the level of ~90%. This high efficiency is achieved *via* combined effects of NRET and RET whose relative roles change with the wavelength. We assessed separate contributions from these ET channels experimentally by comparing PL decays of NQDs on bare Si substrates and on substrates with a thin SiO_2 spacer layer. We found NRET to be a dominant contribution for proximal NQDs in the middle of the visible range but become comparable with RET toward the NIR. At larger distances from the Si substrate, RET serves as a major ET mechanism. As ET can be as effective into ultrathin Si nanomembranes,[5] our current observations show that the ET-based strategy is a viable proposition for NIR absorbing/emitting fluorophores that are optimally tailored for light harvesting in thin-film solar cells. In thin-film PV devices, NQD excitons may effectively excite waveguiding electromagnetic modes propagating within the Si film. Even in this range of weak Si absorption, these modes will then eventually decay into electron—hole pairs, without demanding the film to be thick. NQD-sensitized thin-film Si structures thus emerge as promising candidates for PV devices harvesting solar energy across the spectrum of wavelengths. Their actual potential and achievable conversion efficiencies should be further explored in practically oriented structures with optically thick NQD assemblies.

METHODS

Crystalline Si(111) substrates were used for the experiments. Reference "glass" samples as well as samples with thin interfacial SiO_2 spacer layers were prepared by thermal oxidation in a cleanroom environment. Surface functionalization was based on two approaches depending on the starting surfaces. For oxide-free Si surfaces, a thermal hydrosilylation reaction (200 °C) using ethyl undecylenate molecules on a hydrogenated silicon surface (30 s in 10% HF solution and 150 s in 40% NH_4F solution) was performed, leading to a carboxylic-acid-terminated alkyl chain monolayer after transformation of the head groups.[18] Ethylene diamine was then grafted to the carboxylic acid group in a solution of 1-ethyl-3-(3-dimethylaminopropyl)-carbodiimide (EDC) and 2-(N-morpholino)ethanesulfonic acid (MES).[5,10,29] For silicon oxide (SiO_2) surfaces, the freshly cleaned samples were immersed in a preheated (70 °C) anhydrous toluene solution containing 0.2% of triethoxysilyl undecanal (C11-Ald) molecules for 12 h in a recirculation glovebox (anhydrous conditions). Organic soluble colloidal NQDs emitting at the range from $\lambda \simeq 545$ nm to $\lambda \simeq 800$ nm were purchased from Invitrogen. Immediately before grafting, NQD solutions were diluted to the required concentrations necessary to obtain desired NQD surface coverage in order to avoid ligand detachment commonly observed in aged dilutions. All functionalized surfaces have an amine group as an active group used for the NQD attachment. The latter was performed by immersing samples in a solution of 2 mL of hexane with 7 μL of a stock NQD solution for 1.5 h. Samples with grafted NQDs were then immersed in a solution of 1,6-hexanediamine for 1.5 h to improve NQD passivation. Samples were sonicated in toluene and rinsed at least twice with deionized water (DIW) and dried under the N_2 gas. PL spectra of NQDs grafted on all surfaces looked similar with no "deep trap" PL emission features at longer wavelengths. The measured ellipsometric thicknesses of SAM molecules employed in these attachments were approximately 1.7 nm. As described in our previous work,[10] these concentrations correspond to submonolayer NQD coverages in order to minimize interdot-NRET effects that typically complicate data interpretation.

For spectroscopic studies, we used a microscope-based time-resolved PL system. Samples were mounted on the microscope table and excited at 405 nm by 50 ps laser pulses at 2.5 MHz from a Picoquant diode laser. Excitation was focused on the sample *via* NA = 0.6 objective that also ensured a high photon collection efficiency necessary to obtain PL signatures from a submonolayer of NQDs. The collected emission was passed through a spectrometer and directed either to a CCD camera for spectral analysis or to a sensitive photon detector (MicroPhoton Devices) for the wavelength-dependent PL lifetime detection. PL decays were collected *via* the time-correlated single photon counting (TCSPC) performed on board the Pico300E photon counting hardware (PicoQuant GmbH). The overall time resolution was better than 70 ps.

Conflict of Interest: The authors declare no competing financial interest.

REFERENCES AND NOTES

1. Würfel, P. *Physics of Solar Cells. From Principles to New Concepts*; Wiley-VCH: Weinheim, Germany, 2005.
2. Green, M. A. *Third Generation Photovoltaics. Advanced Solar Energy Conversion*; Springer-Verlag: Berlin, 2003.
3. *Organic Photovoltaics: Mechanisms, Materials, and Devices*; Sun, S. S., Sariciftci, N. S., Eds.; CRC Press: Boca Raton, FL, 2005.
4. Polman, A.; Atwater, H. Photonic Design Principles of Ultrahigh-Efficiency Photovoltaics. *Nat. Mater.* **2012**, *11*, 174–177.
5. Nguyen, H. M.; Seitz, O.; Peng, W.; Gartstein, Y. N.; Chabal, Y. J.; Malko, A. V. Efficient Radiative and Nonradiative Energy Transfer from Proximal CdSe/ZnS Nanocrystals into Silicon Nanomembranes. *ACS Nano* **2012**, *6*, 5574–5582.
6. McDonald, S.; Konstantatos, G.; Zhang, S.; Cyr, P. W.; Klem, E. J. D.; Levina, L.; Sargent, E. H. Solution-Processed PbS

Quantum Dot Infrared Photodetectors and Photovoltaics. *Nat. Mater.* **2005**, *4*, 138–142.

7. Ip, A. H.; Thon, S. M.; Hoogland, S.; Voznyy, O.; Zhitomirsky, D.; Debnath, R.; Levina, L.; Rollny, L. R.; Carey, G. H.; Fischer, A.; *et al.* Hybrid Passivated Colloidal Quantum Dot Solids. *Nat. Nanotechnol.* **2012**, *7*, 577–582.

8. Lu, S.; Lingley, Z.; Asano, T.; Harris, D.; Barwicz, T.; Guha, S.; Madhukar, A. Photocurrent Induced by Nonradiative Energy Transfer from Nanocrystal Quantum Dots to Adjacent Silicon Nanowire Conducting Channels: Toward a New Solar Cell Paradigm. *Nano Lett.* **2009**, *9*, 4548–4552.

9. Andreakou, P.; Brossard, M.; Bernechea, M.; Konstantatos, G.; Lagoudakis, P. Resonance Energy Transfer from PbS Colloidal Quantum Dots to Bulk Silicon: The Road to Hybrid Photovoltaics. *Proc. SPIE* **2012**, *8256*, 82561L/1–6.

10. Nguyen, H. M.; Seitz, O.; Aureau, D.; Sra, A.; Nijem, N.; Gartstein, Y. N.; Chabal, Y. J.; Malko, A. V. Spectroscopic Evidence for Nonradiative Energy Transfer between Colloidal CdSe/ZnS Nanocrystals and Functionalized Silicon Substrates. *Appl. Phys. Lett.* **2011**, *98*, 161904/1–3.

11. Stavola, M.; Dexter, D. L.; Knox, R. S. Electron−Hole Pair Excitation in Semiconductors *via* Energy Transfer from an External Sensitizer. *Phys. Rev. B* **1985**, *31*, 2277–2289.

12. Novotny, L.; Hecht, B. *Principles of Nano-Optics*; Cambridge University Press: Cambridge, 2006.

13. Aspnes, D. E.; Studna, A. A. Dielectric Functions and Optical Parameters of Si, Ge, GaP, GaAs, GaSb, InP, InAs, and InSb from 1.5 to 6.0 eV. *Phys. Rev. B* **1983**, *27*, 985–1009.

14. Pons, T.; Medintz, I. L.; Sykora, M.; Mattoussi, H. Spectrally Resolved Energy Transfer Using Quantum Dot Donors: Ensemble and Single-Molecule Photoluminescence Studies. *Phys. Rev. B* **2006**, *73*, 245302/1–7.

15. Li, M.; Cushing, S. K.; Wang, Q.; Shi, X.; Hornak, L. A.; Hong, Z.; Wu, N. Size-Dependent Energy Transfer between CdSe/ZnS Quantum Dots and Gold Nanoparticles. *J. Phys. Chem. Lett.* **2011**, *2*, 2125–2129.

16. Chance, R. R.; Prock, A.; Silbey, R. In *Advances in Chemical Physics*; Rice, S. A., Prigogine, I., Eds.; Wiley: New York, 1978; Vol. 37, pp 1−65.

17. Aureau, D.; Varin, Y.; Roodenko, K.; Seitz, O.; Pluchery, O.; Chabal, Y. J. Controlled Deposition of Gold Nanoparticles on Well-Defined Organic Monolayer Grafted on Silicon Surfaces. *J. Phys. Chem. C* **2010**, *114*, 14180–14186.

18. Seitz, O.; Dai, M.; Aguirre-Tostado, F. S.; Wallace, R. M.; Chabal, Y. J. Copper-Metal Deposition on Self Assembled Monolayer for Making Top Contacts in Molecular Electronic Devices. *J. Am. Chem. Soc.* **2009**, *131*, 18159–18167.

19. Seitz, O.; Fernandez, P. G.; Mahmud, G. A.; Wen, H.-C.; Stiegler, H. J.; Chapman, R. A.; Vogel, E. M.; Chabal, Y. J. One-Step Selective Chemistry for Silicon-on-Insulator Sensor Geometries. *Langmuir* **2011**, *27*, 7337–7340.

20. Waldeck, D. H.; Alivisatos, A. P.; Harris, C. B. Nonradiative Damping of Molecular Electronic Excited States by Metal Surfaces. *Surf. Sci.* **1985**, *158*, 103–125.

21. Herzinger, C. M.; Johs, B.; McGahan, W. A.; Woollam, J. A.; Paulson, W. Ellipsometric Determination of Optical Constants for Silicon and Thermally Grown Silicon Dioxide *via* a Multi-Sample, Multi-Wavelength, Multi-Angle Investigation. *J. Appl. Phys.* **1998**, *83*, 3323–3336.

22. Agranovich, V. M.; Galanin, M. D. *Electronic Excitation Energy Transfer in Condensed Matter*; Elsevier: Amsterdam, 1982.

23. Agranovich, V. M.; Gartstein, Y. N.; Litinskaya, M. Hybrid Resonant Organic−Inorganic Nanostructures for Optoelectronic Applications. *Chem. Rev.* **2011**, *111*, 5179–5124.

24. Wuister, S. F.; de Mello Donegá, C.; Meijerink, A. Influence of Thiol Capping on the Exciton Luminescence and Decay Kinetics of CdTe and CdSe Quantum Dots. *J. Phys. Chem. B* **2004**, *108*, 17393–17397.

25. Fröhlich, H. *Theory of Dielectrics*; Clarendon Press: Oxford, 1949.

26. Thränhardt, A.; Ell, C.; Khitrova, G.; Gibbs, H. M. Relation between Dipole Moment and Radiative Lifetime in Interface Fluctuation Quanatum Dots. *Phys. Rev. B* **2002**, *65*, 035327/1–6.

27. Wuister, S. F.; de Mello Donegá, C.; Meijerink, A. Local-Field Effects on the Spontaneous Emission Rate of CdTe and CdSe Quantum Dots in Dielectric Media. *J. Chem. Phys.* **2004**, *121*, 4310–4315.

28. Atwater, H. A.; Polman, A. Plasmonics for Improved Photovoltaic Devices. *Nat. Mater.* **2010**, *9*, 205–213.

29. Seitz, O.; Caillard, L.; Nguyen, H. M.; Chiles, C.; Chabal, Y. J.; Malko, A. V. Optimizing Non-radiative Energy Transfer in Hybrid Colloidal−Nanocrystal/Silicon Structures by Controlled Nanopillar Architectures for Future Photovoltaic Cells. *Appl. Phys. Lett.* **2012**, *100*, 021902/1–4.